iScience, Volume *27*

Supplemental information

Polysphaeroides filiformis, a proterozoic cyanobacterial microfossil and implications for cyanobacteria evolution

Catherine F. Demoulin, Marie Catherine Sforna, Yannick J. Lara, Yohan Cornet, Andrea Somogyi, Kadda Medjoubi, Daniel Grolimund, Dario Ferreira Sanchez, Remi Tucoulou Tachoueres, Ahmed Addad, Alexandre Fadel, Philippe Compère, and Emmanuelle J. Javaux

Table S1. Fossil occurrence of *P. filiformis* during the Precambrian, related to introduction.

Country	Group	Formation	Ages (Ga)	Environments	References
Siberia	Billyakh	Ust'-Il'ya	1.483 ± 0.1	Deepest water of terrigenous shelf deposits influenced by storm	[1]
Siberia	Billyakh	Kotuikan	1.457 ± 0.220	Open-sea on carbonate platform	[1, 2]
Democratic Republic of Congo	Mbuji-Mayi	BIIc6	1.04-1.006	Photic shallow-water	[3]
Siberia	Miroedikha	Miroedikha	0.95-0.85	Transgressive complex: shallow-water to deepwater	[4]
North China	Tumen	Shiwangzhuang	0.85 ± 0.25	Tidal flat environment	[5]
East European Platform	/	Vychegda	0.635-0.55	Shallow water	[6]

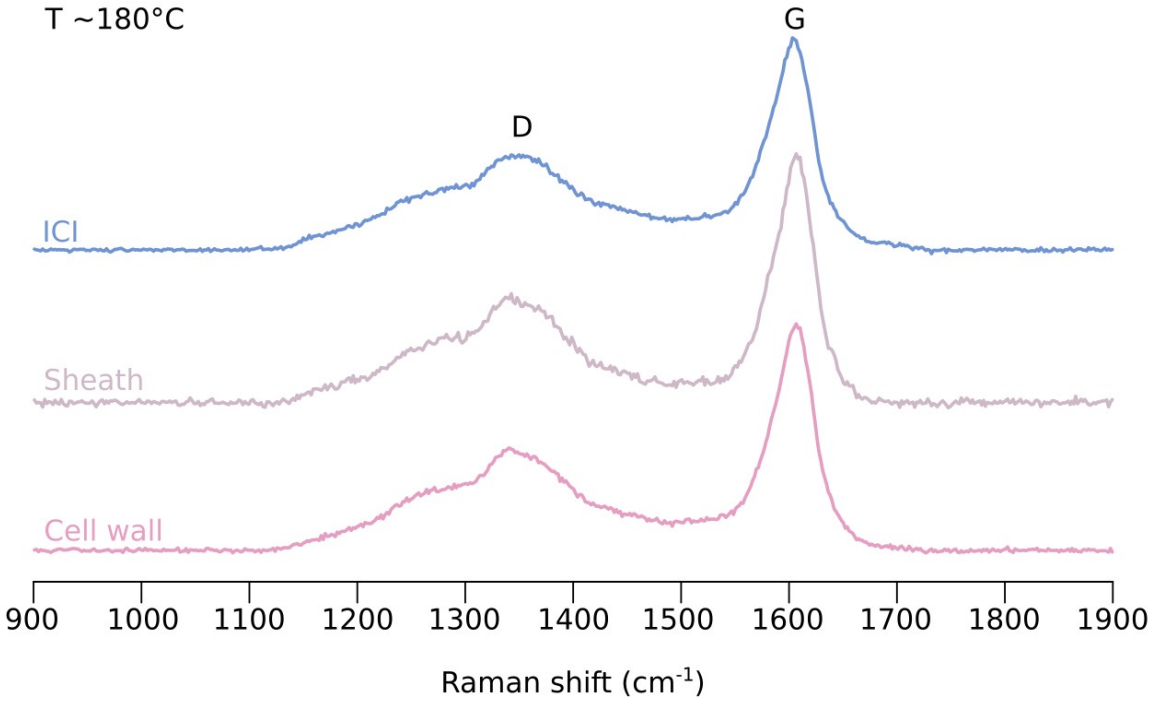

Figure S2. Representative Raman spectra for the sheath, cell walls and ICIs of *P. filiformis*, related to the STAR methods and Table S3. The D (disordered carbon band) and G (graphite band) bands are at the same position for all spectra, demonstrating the syngenicity of these structures. Moreover, the metamorphism temperature (~180 °C) was calculated using the Raman Reflectance technique [7]. A total of 10 points were measured on several ICI, cell walls and on the sheath on one filament of *P. filiformis* and gave a mean temperature of 182.96 ± 2.33°C (sheath), 180.86 ± 2.88°C (cell wall), 179.02 ± 2.05°C (ICI).

Table S3. Raman data obtained for sheath, cell wall and ICI of *P. filiformis*, related to STAR methods and Figure S2. Raman positions (ω in cm^{-1}) and full width at half maximum height (FWHM in cm^{-1}) of bands D1 (disordered carbon band) and G (graphite band) (in cm^{-1}).

Raman reflectance: RmcR0=0.0537*(ωG-ωD1)-11.21.
Calculated temperatures (T°C RmcR0 = (LN(RmcRo+1.68)/0.0124)) [7] on sheath, cell walls and ICIs.

Sheath	FWHM D1	FWHM G	ω D1	ω G	RmcR0	T°C RmcR0
	94,94	48,64	1359	1602	1,83	184,42
	94,25	48,64	1359	1602	1,84	184,44
	95,12	48,22	1359	1602	1,83	184,17
	91,23	49,01	1360	1601	1,77	181,38
	92,90	48,68	1359	1601	1,77	181,42
	92,30	48,51	1360	1601	1,72	179,22
	94,17	47,77	1359	1602	1,83	184,07
	90,95	48,40	1360	1601	1,74	180,35
	95,09	48,93	1360	1602	1,81	183,26
	95,77	48,19	1359	1603	1,89	186,95
Mean	**93,67**	**48,50**	**1359**	**1602**	**1,80**	**182,97**
σ	**1,72**	**0,37**	**0,50**	**0,74**	**0,05**	**2,33**
Cellwall	**FWHM D1**	**FWHM G**	**ω D1**	**ω G**	**RmcR0**	**T°C RmcR0**
	90,05	47,75	1359	1600	1,73	179,83
	85,52	48,57	1360	1602	1,79	182,31
	85,42	47,09	1359	1599	1,69	177,61
	85,73	48,23	1359	1600	1,75	180,61
	82,65	47,03	1360	1600	1,70	178,13
	87,64	48,09	1359	1602	1,82	183,99
	83,92	47,91	1360	1600	1,68	177,28
	86,43	46,36	1358	1599	1,73	179,76
	85,34	47,55	1358	1601	1,81	183,46
	87,50	49,39	1359	1602	1,86	185,64
Mean	**86,02**	**47,80**	**1359**	**1600**	**1,76**	**180,86**
σ	**2,06**	**0,86**	**0,61**	**1,13**	**0,06**	**2,88**
ICI	**FWHM D1**	**FWHM G**	**ω D1**	**ω G**	**RmcR0**	**T°C RmcR0**
	83,30	47,93	1360	1600	1,68	177,51
	84,88	48,15	1360	1601	1,74	180,21
	87,06	48,09	1360	1601	1,73	179,69
	84,50	46,91	1359	1598	1,62	174,62
	83,65	48,62	1360	1602	1,76	181,15
	84,24	47,59	1359	1600	1,74	180,07
	83,35	48,23	1360	1602	1,76	181,14
	84,23	48,38	1360	1600	1,68	177,21
	85,07	47,65	1360	1600	1,71	178,67
	84,42	47,24	1359	1600	1,74	179,95
Mean	**84,47**	**47,88**	**1360**	**1600**	**1,72**	**179,02**
σ	**1,09**	**0,53**	**0,55**	**1,04**	**0,04**	**2,05**

Table S4. Numerical values for dimensions of sheath, trichome and cells of the microfossil *Polysphaeroides filiformis* and the four modern strains selected for the comparison, *Stigonema robustum, Stigonema turfaceum*, *Stigonema informe* and *Bangiopsis franklynottii*, related to Figure 1 and STAR methods.

Species		Sheath width (µm)	Trichome width (µm)	Cells diameter (µm)
P. filiformis	Max	75.7	51.1	28.8
(n=30)	Min	38.6	14.2	5.5
	Mean	56.2	30.9	11.2
	SD	9.1	7.2	3.5
S. robustum CBFS-A027	Max	108.8	46.1	25.8
(n=12)	Min	32.8	31.9	8.6
	Mean	54.3	41.3	14.8
	SD	22.6	6.5	4.1
*S. turfaceum*CBFS-A034	Max	46.4	22.8	18.9
(n=19)	Min	21.5	12.3	8.1
	Mean	31	17.3	11.9
	SD	6.3	3.4	4.2
*S. informe*CBFS-A033	Max	62.9	52.1	14.6
(n=12)	Min	25.5	14.9	5.5
	Mean	44.9	33.7	9.2
	SD	10.6	11.2	2.5
B. franklynottii CCMP3416	Max	44.7	35.5	12.1 x 14
(n=22)	Min	10	9.5	4.7 x 6.2
	Mean	24.7	18.9	8.5 x 10
	SD	8.6	6.7	1.8 x 2.1

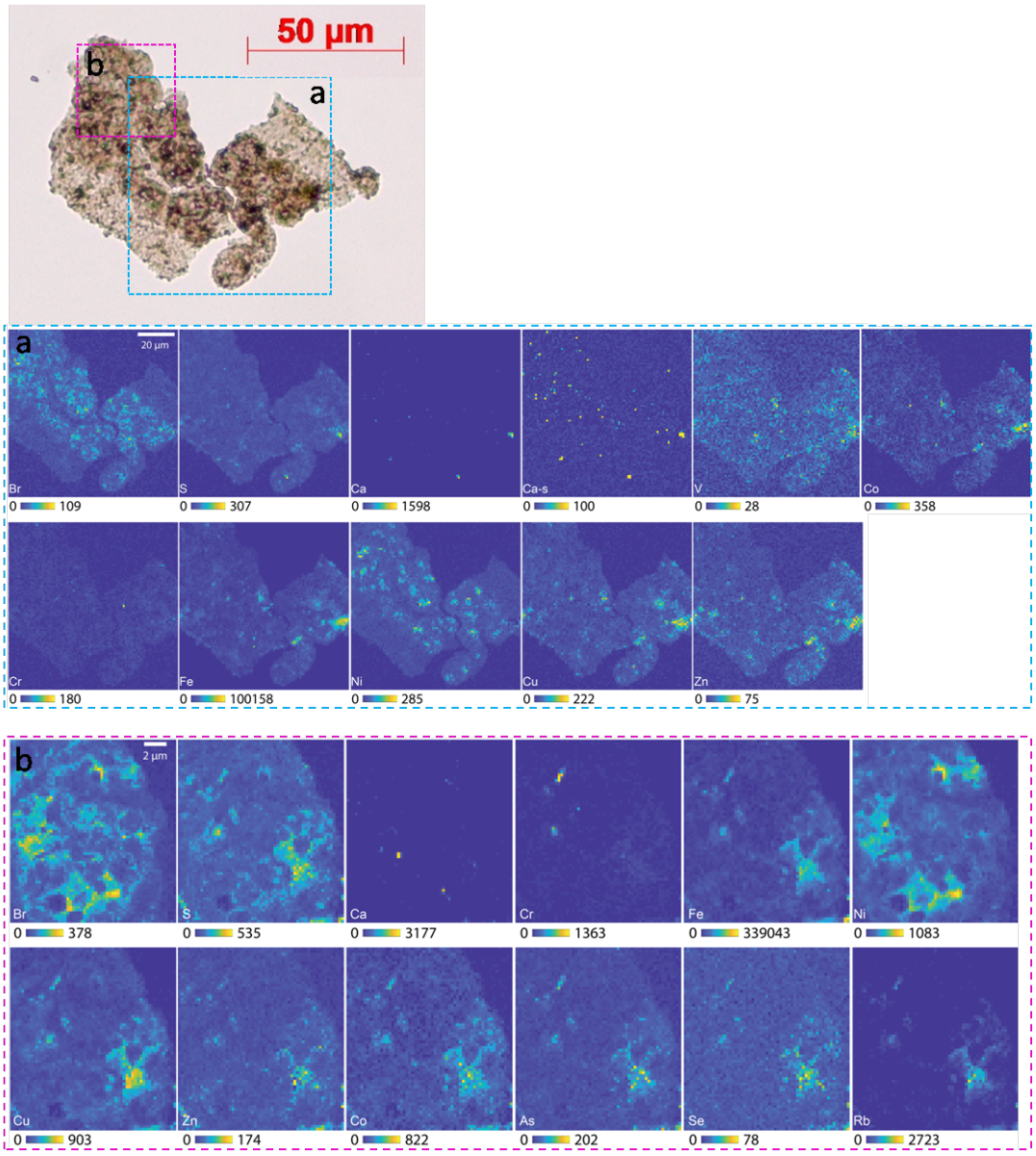

Figure S5. **Photomicrograph of *P. filiformis* and its SR-nanoXRF maps, related to Figure 2.** These SR-nanoXRF maps show the distribution of several elements in two locations **(a)** blue area and **(b)** pink area on the microfossil. The map of Ni show that the distribution of this element is mainly within ICIs. These maps were obtained at ESRF synchrotron (energy 17.5 keV).

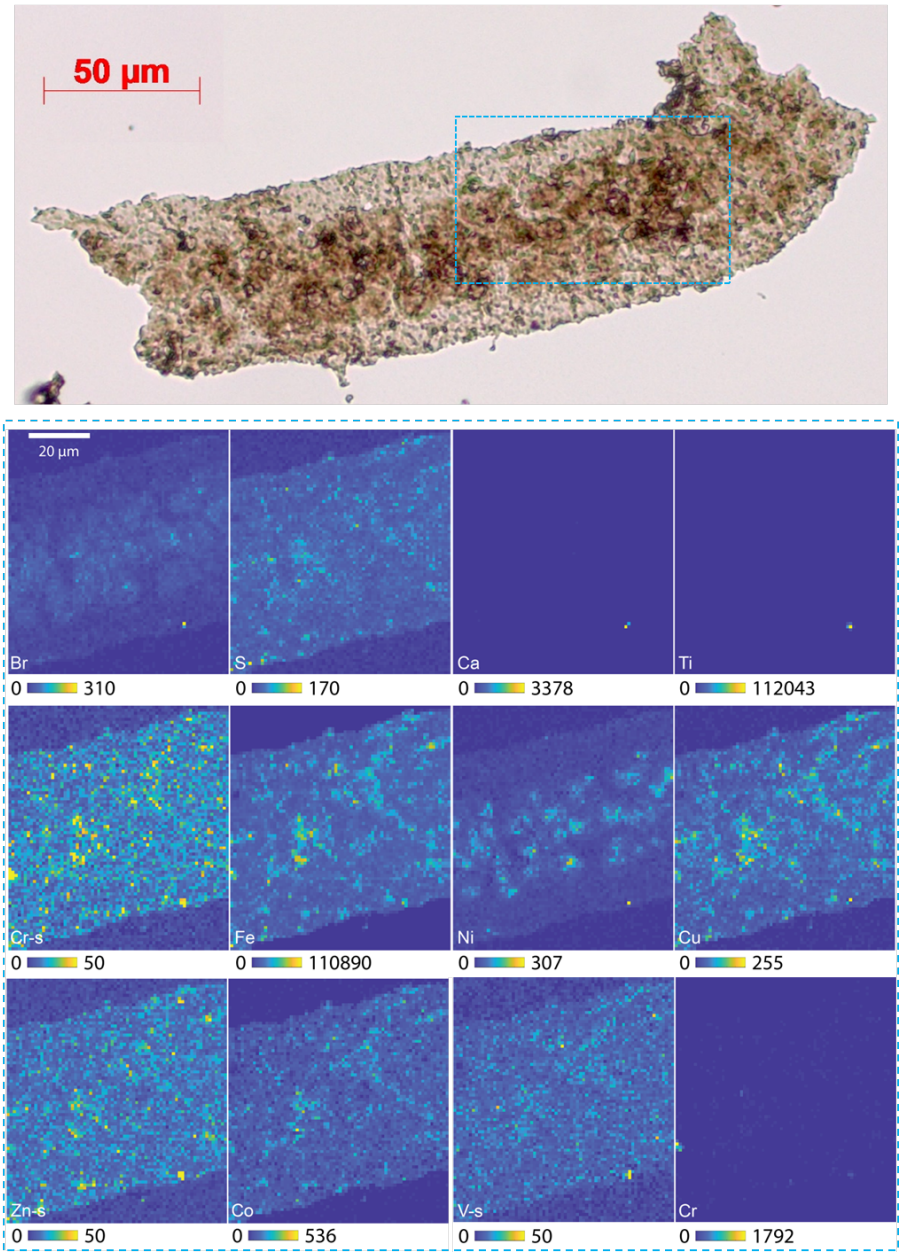

Figure S6. Photomicrograph of *P. filiformis* and its SR-nanoXRF maps, related to Figure 2. These SR-nanoXRF maps show the distribution of several elements and highlight that the distribution of Ni is mainly within ICIs(blue area). These maps were obtained at ESRF synchrotron (energy 17.5 keV).

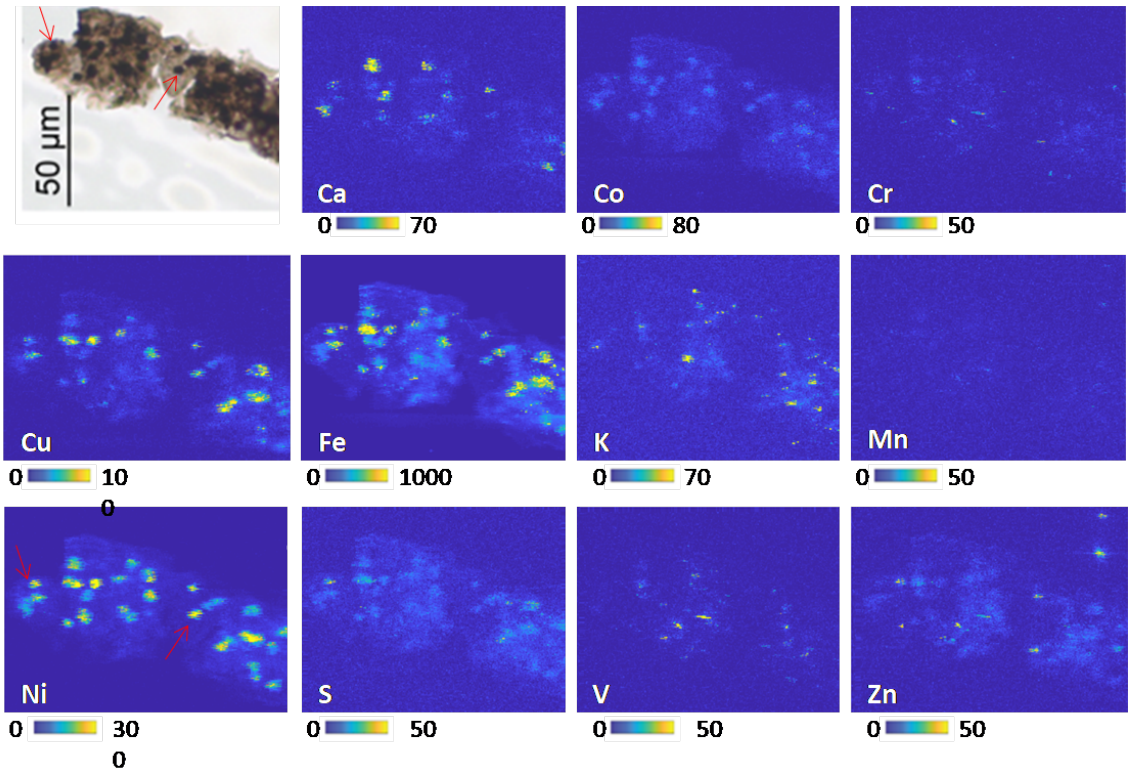

Figure S7. Photomicrograph of *P. filiformis* and its SR-nanoXRF maps, related to Figure 2. These SR-nanoXRF maps show the distribution of several elements and highlight that the distribution of Ni and Co is mainly within ICIs. They also show a distribution of Ca and Cu within ICIs for this specimen. These maps were obtained at Soleil synchrotron (energy 12 keV).

Table S8. Counts of Ni in the sheath, cell wall and ICIs of *P. filiformis* and the ratios between ICI and the cell wall and between ICI and the sheath, showing the enrichment of Ni mainly in ICI, related to Figure 2.

Ni counts in sheath ($cts.s^{-1}$)	Ni counts in cell wall ($cts.s^{-1}$)	Ni counts in ICI ($cts.s^{-1}$)	ICI/cell wall	ICI/sheath
0.00035	0.0006	0.0048	7.96	11.11
0.00034	0.00069	0.0039	5.7	14.29
0.000054	0.00011	0.0029	26.74	53.87
0.00012	0.00012	0.0018	18.29	16.45

Table S9. Parameters and results for the estimation of tetrapyrrole molar concentration in *P. filiformis* ICIs, related to Figure 3.
$^{a}V_{cell}=(4 .\pi .R_m^3)/3$; $^{b}A_p=\pi.R_m^2$; $^{c}m_{Ni}= (AD_{Ni}).ICI .0.1 . A_p$; $^{d}n_{Ni}=m_{Ni}/M_{Ni}$; $^{e}C_{tetrapyrrole}= n_{Ni}/V_{cell}$; [8]

Cells	Radius R_m (mm)	Volume V_{cell}[a] (mm^3)	% ICI in cell ICI	Projected area of the cell A_p[b] (mm^2)	Mean count rate (counts/s)	Measured area density of Ni in the ICI AD_{Ni} (g/mm^2)	Calculated Ni mass m_{Ni}[c] (g)	Corresponding number of mole for Ni n_{Ni}[d] (mol)	Molar concentration of tetrapyrrole $C_{tetrapyrrole}$[e] (pM)
1	0.00723	$1.58 .10^{-6}$	41.67	0.00016	10.49	$2.87 .10^{-17}$	$1.97 .10^{-21}$	$3.35 .10^{-23}$	21.16
2	0.00784	$2.02 .10^{-6}$	37.56	0.00019	20.15	$5.51 .10^{-17}$	$4 .10^{-21}$	$6.81 .10^{-23}$	33.79
3	0.00594	$8.79 .10^{-7}$	42.72	0.00011	14.64	$4 .10^{-17}$	$1.90 .10^{-21}$	$3.23 .10^{-23}$	36.81
4	0.00855	$2.57 .10^{-6}$	4421	0.00023	20.13	$5.51 .10^{-17}$	$5.53 .10^{-21}$	$9.42 .10^{-23}$	36.61
5	0.00803	$2.17 .10^{-6}$	26.63	0.00020	17.12	$4.6.10^{-17}$	$2.53 .10^{-21}$	$4.31 .10^{-23}$	19.85
6	0.00758	$1.83 .10^{-6}$	26.03	0.00018	2.09	$5.72 .10^{-18}$	$2.69 .10^{-22}$	$4.59 .10^{-24}$	2.51
7	0.00911	$3.17 .10^{-6}$	24.79	0.00026	3.95	$1.08 .10^{-17}$	$6.99 .10^{-22}$	$1.19 .10^{-23}$	3.76

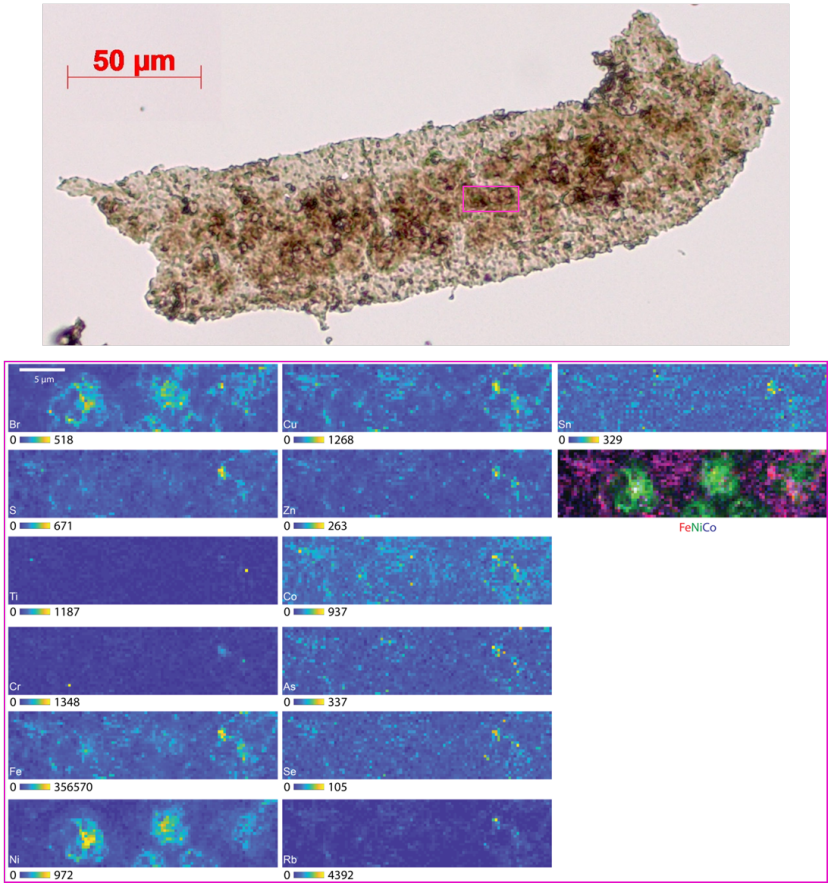

Figure S10. Photomicrograph of *P. filiformis* and its SR-µXRF maps, related to Figure 2. These SR-µXRF maps are focused on five ICIs and show the distribution of several elementsand particularly highlight that the distribution of Ni is mainly within ICIs (pink area). These maps were obtained at SLS synchrotron (energy 8.4 keV).

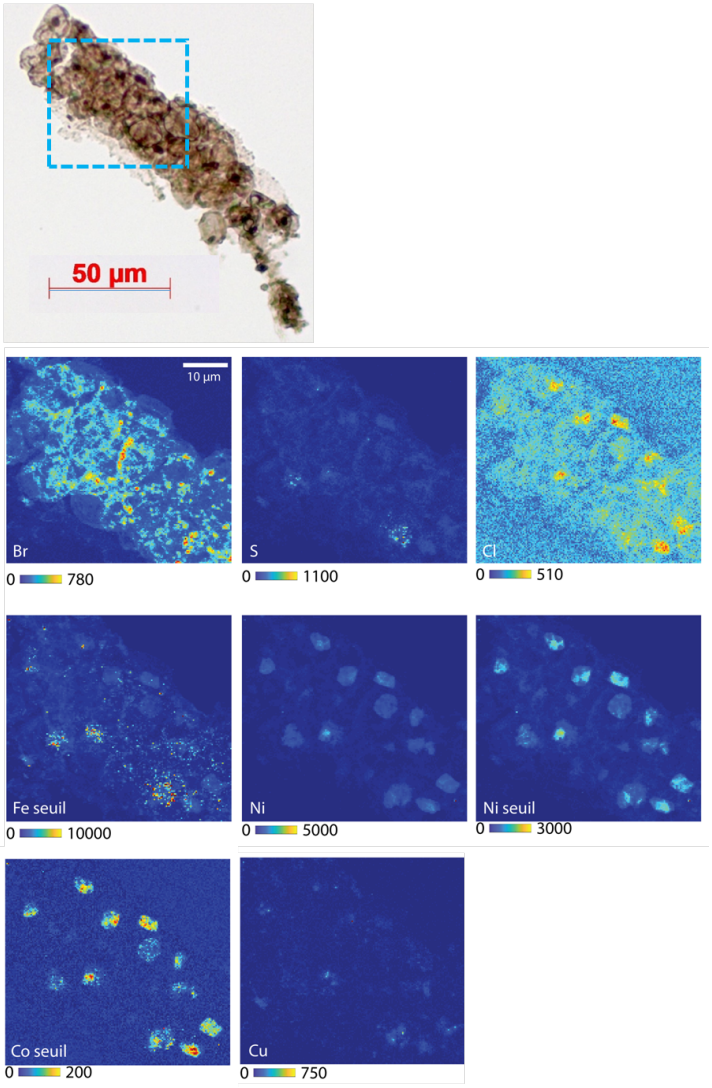

Figure S11. Photomicrograph of *P. filiformis* and its SR-nanoXRF maps, related to Figure 2. These SR-nanoXRF maps show the distribution of several elements and highlight that the distribution of Ni and Co is mainly within ICIs (blue area). These maps were obtained at ESRF synchrotron (energy 17.5 keV).

Table S12. Linear combination fitting results for Ni K-edge spectra of XANES, related to Figure 3.

Analysis point	NiOEP	NiTPP	Asphaltene	NiO	Ni3S2	Sum	R factor	Total porphyrinic species ratio
Point 1	37.4 %	15.4 %	12.6 %	12.4 %	29.1 %	106.9 %	0.0022	65.4 %
Point 2	41.4 %	0 %	11.3 %	10.9 %	46.3 %	109.8 %	0.0026	52.7 %
Point 1 2019	46 %	15.8 %	28.8 %	5.1 %	0 %	95.7 %	0.0012	90.6 %
Point 2 2019	34.8 %	22.4 %	25.5 %	14.4 %	0 %	97.1 %	0.0013	82.7 %
Point 3 2019	44.8 %	16.3 %	14.5 %	17 %	0 %	92.6 %	0.0010	75.6 %

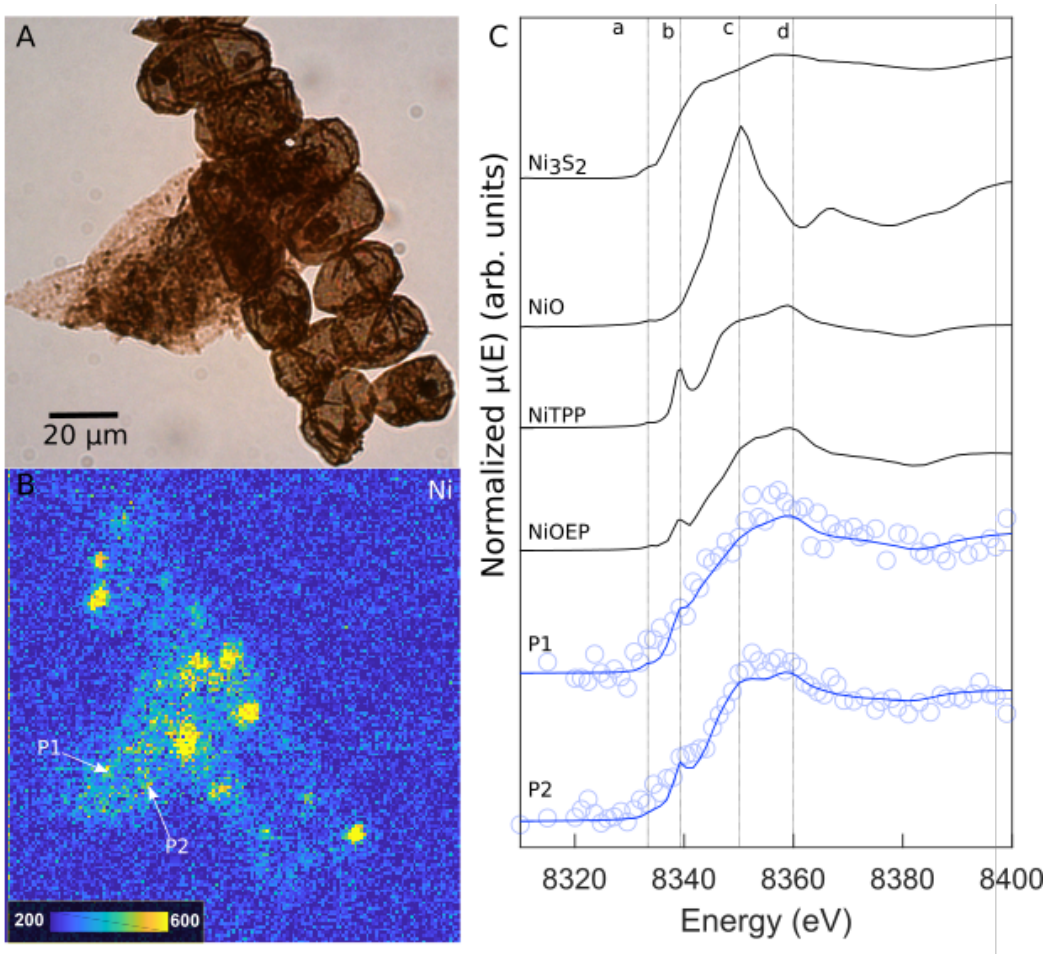

Figure S13. Ni-geoporphyrin SR-nanoXRF and SR-µXANES spectra measured in two ICIs of *P. filiformis,* related to Figure 3. (A) Microphotograph of *P. filiformis* (located below another microfossil), **(B)** SR-XRF map showing enrichment of Ni within ICIs. **(C)** SR-µXANES spectra obtained at SLS synchrotron on a specimen of *P. filiformis* and on two Ni-enriched ICIs (point 1 & 2) at Ni K-edge. These spectra were compared to spectra of Ni inorganic (NiO and Ni3S2) and organic (NiOEP; NiTPP and Asphaltene) standards. The four lines (a, b, c and c – dotted lines) are typical of spectrum shape of Ni in coordination (IV) in Ni-porphyrins. Data (blue stars) obtained for ICIs of the microfossil and their fitted spectra may have differences due to the molecular heterogeneities between inorganic and organic standards used for the linear combination fitting and the incorporated tetrapyrroles moieities in kerogen.

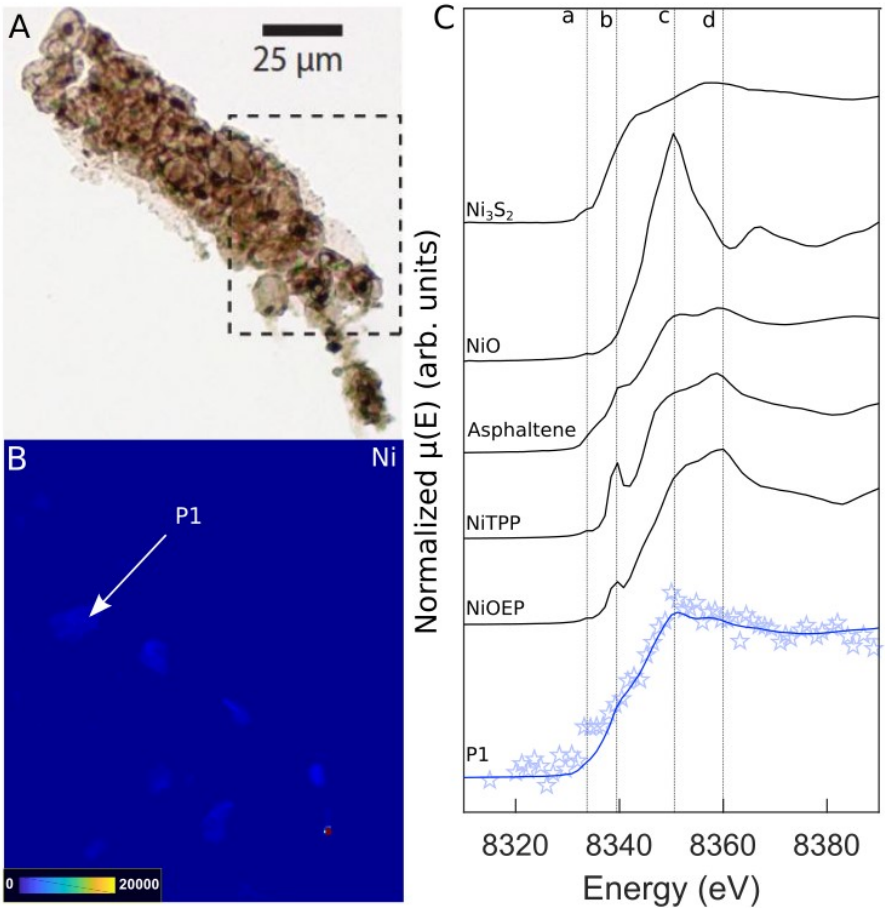

Figure S14. Ni-geoporphyrin SR-nanoXRF and SR-µXANES spectra measured in an ICI of *P. filiformis,* related to Figure 3. (A) Microphotograph of *P. filiformis,* **(B)** SR-XRF map showing enrichment of Ni within ICIs (black area)**. (C)** SR-µXANES spectra obtained at SLS synchrotron on a specimen of *P. filiformis* and on one Ni-enriched ICI (point 1) at Ni K-edge. This spectrum was compared to spectra of Ni inorganic (NiO and Ni3S2) and organic (NiOEP; NiTPP and Asphaltene) standards. The four lines (a, b, c and c – dotted lines) are typical of spectrum shape of Ni in coordination (IV) in Ni-porphyrins. Data (blue stars) obtained for ICIs of the microfossil and their fitted spectra may have differences due to the molecular heterogeneities between inorganic and organic standards used for the linear combination fitting and the incorporated tetrapyrroles moieities in kerogen.

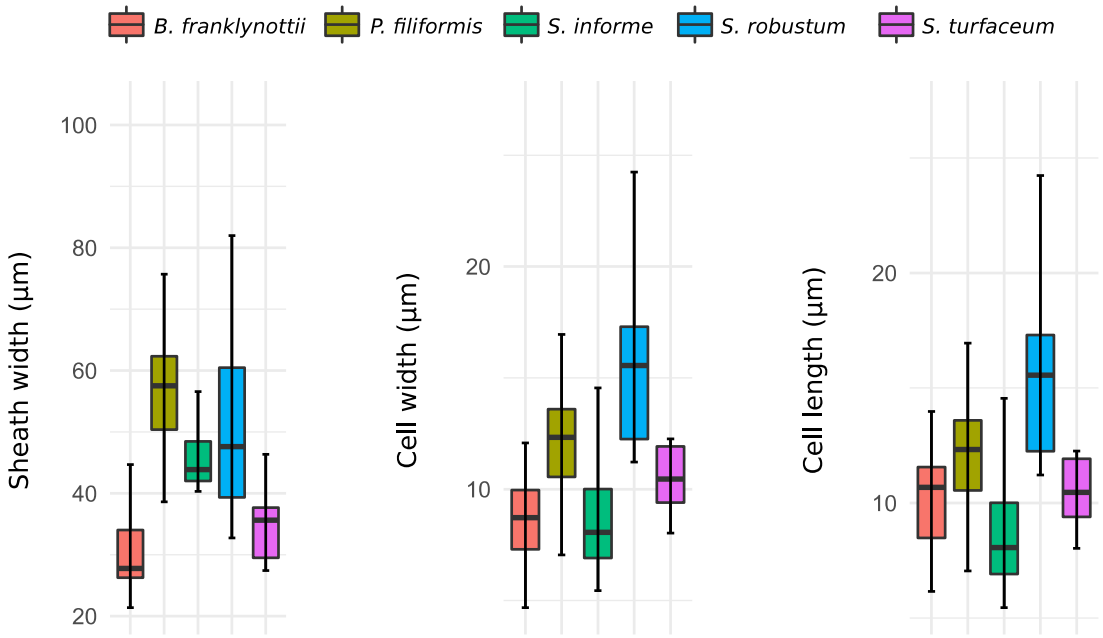

Figure S15. Boxplot of sheath width, cell width and cell length of fossil *P. filiformis* (n=30) and modern red alga *B franklynottii* CCMP3416 (n=22) and cyanobacteria *S. informe* CBFS-A033 (n=12), *S. robustum* CBFS-A027 (n=12), *S. turfaceum* CBFS-A034 (n=19), related to Figure 1 and Table S4 for measurements.

Table S16. Tentative of bands assignment for FT-IR spectra of *Polysphaeroides filiformis*, *Calothrix sp*. BCCM/ULC003, *Stigonema ocellatum* SAG48.90 and *Bangiopsis franklynottii* CCMP3416, related to Figure 5.

Bands (cm^{-1}) on micro-FTIR spectra of the studied specimens				Tentative bands assignment
P. filiformis	*Calothrix* sp. BCCM/ULC003	*S. ocellatum* SAG48.90	*B. franklynottii* CCMP3416	
			687s	-CH out of plane bend [9]
		718w		-CH out of plane bend [9]
	747mw	742w		-CH out of plane bend [9]
750w				=C-H aromatic deformation [10]
		788w		-CH out of plane bend [9]
802m				=C-H aromatic deformation [11]
	826mw			-CH out of plane bend [9]
		844w		-CH out of plane bend [9]
			850m	α glycosidiclinkage [12]
		872w		-CH out of plane bend [9]
879w				=C-H aromatic deformation [10]
		890mw		β glycosidiclinkage [12]
	897w			Antisymmetrical out of phase stretching [13]
			928m	C-O vibrations of the 3,6anhydro-bridge (galactose) [12]
		934m		C-O-C[9]
	965sh	967mw		C-O, C-C [9]
		990mw		C–O–C stretching[15]
1002ms			**1006vs**	C–O–C stretching etheric bonds in the glucopyranose ring [14]; deformation vibration C-O secondary alcohols [16]
	1032vs*	1044s		C–O–C stretching etheric bonds in the glucopyranose ring [14]
1079vs	1073s	**1074vs**	1074sh	C–O–C stretching etheric bonds in the glucopyranose ring [14]; deformation vibration C-O secondary alcohols (16); 3,6-anhydrobridge if shoulder in red algae (17)
		1114ms		C–O–C stretching etheric bonds in the glucopyranose ring [14]
1136ms	1138ms			deformation vibration C-O secondary alcohols [16]
	1165ms	1151ms	1148m	C-O stretching [18]; skeletal vibration of the polygalactane [19]; CC ring stretching breathing pyrrole in scytonemin [22]
		1179sh		C-O stretching [18]
1193sh				deformation vibration in phenols, ether [16]

1202sh	1202sh			C-O-C stretching of polysaccharides [15]; C-O stretching, Phenol [20, 21]
			1206m	S=O stretching [18]
		1247mw		P=O stretching in nucleic acids [15]
1261m				deformation vibration C-O in aryl ethers [16]; (C=C-C=C) system stretching (trans) in scytonemin [22]
	1272m			(CC) stretching of aromatic ring: *p*-disubstituted benzenes in scytonemin [22]
	1319m*	1314w		C-H stretch, N-H bend in proteins [18]; C=N stretch in indole ring of scytonemin [22]
			1335w	SO_2 out-of-phase stretching [23]
	1372m*	1375mw		-CH2, -CH3, C-O bending in proteins and carboxylic groups [18]; stretch of indole ring in scytonemin [24]
			1406s	C-O carboxylic group stretching [18]
		1417mw		C-O carboxylic group stretching [18]
1432ms				asymmetric stretching –CH3 –CH2 [16]; C=CH bending modes in scytonemin [22]
	1449m*			stretching C=CH in scytonemin [22]
	1454m*			(N=C-C=C) ring stretching in scytonemin [24]
		1462mw	1463s	C-O stretching of carboxylic group [18]; -CH3 bending [12]
1466sh				asymmetric stretching –CH3 –CH2 [16]
	1514m*			(N=C-C=C) ring stretching in scytonemin [22]
1534m				aliphatic COOH (as *sh*) in [10]
	1544ms	1545m	1541s	N-H bend of amide II [15]
	1587ms*			Aromatic groups C=C [11]; C-CH aromatic ring quadrant stretching in scytonemin [22]
1594m				C-C aromatic ring stretching [10]
1625sh				aromatic C=C [16]; C=CH stretching attached to cyclopentene ring in scytonemin [22]
	1637ms	1634s	1633s	C=O stretching amide I [12, 15]; C=CH stretching attached to cyclopentene ring in scytonemin[22]
	1653ms	1655s		C=O stretching amide I [25]; C=C stretching conjugated (trans) in scytonemin [22]
1671w				Conjugated C=O [16]
			1681s	C=O stretching ester groups [18]
	1707mw			C=O stretching ester groups [25]
1730w		1730ms		saturated aliphatic (–COO–R) [26]; C=O stretching [14, 21]
			1743ms	C=O stretching ester groups [25]
2850	2856	2859	2859	symmetric C-H of CH_2 stretching [10, 15]

	2883	2883	2887	stretching C-H of CH_3 [15]
2918	2929	2929	2929	asymmetric stretching C-H of CH_2[10, 15
2965	2969	2965	2960	asymmetric stretching C-H of CH_3 [15]
3000-3100			3015	OH-N stretching [16]
3100-3370	3000-3660	3000-3680	3000-3700	-OH stretching [12]
3370-3500				OH stretching [10]

*denotes bands that also correspond to scytonemin vibrations; vs is for very strong, s is for strong , m for medium , w is for weak, sh stands for shoulder. Wavenumbers in bold represent the most intense bands of the spectra.

Table S17. Summary data table for the studied fossil and modern organisms, related to Figures 1, 4 and 5.

Organism	Morphology	Size	Ultrastructure	Composition
Polysphaeroides filiformis	Spheroidal vesicles arranged into filament. Branching filament surrounded by a sheath. T-type branching.	*Cells* 5.51 – 28.77 µm; *Trichome width* 14.24 – 51.06 µm; *Sheath width* 38.61 – 75.7 µm	Trilayered sheath with outer and inner electron-dense layers and a middle electron-tenuous layer. Bilayered cell wall with an outer electron-dense layer and an inner electron-tenuous layer.	Mainly composed of polysaccharides comparable to polysaccharides of cyanobacterial sheath. Detection of Ni-porphyrins in ICI interpreted as degraded chlorophyll pigment.
Stigonema informe **CBFS-A033**	Spheroidal vesicles arranged into filament. Branching filament surrounded by a sheath. T-type branching.	*Cells* 5.45 – 14.55 µm; *Trichome width* 14.94 – 52.14 µm; *Sheath width* 2547 – 62.92 µm	/	/
Stigonema robustum **CBFS-A027**	Spheroidal vesicles arranged into filament. Branching filament surrounded by a sheath. T-type branching.	*Cells* 8.62 – 25.82 µm; *Trichome width* 31.88 – 46.09 µm; *Sheath width* 32.75 – 108.75 µm	Trilayered sheath with outer and inner electron-dense layers and a middle electron-tenuous layer. Bilayered cell wall with an outer electron-dense layer and an inner electron-tenuous layer. Cells are embedded in a gel-like matrix and may present an individual envelope.	/
Stigonema turfaceum **CBFS-A034**	Spheroidal vesicles arranged into filament. Branching filament surrounded by a sheath. T-type branching.	*Cells* 8.06 – 18.87 µm; *Trichome width* 12.26 – 22.77 µm; *Sheath width* 21.46 – 46.36 µm	/	/

***Stigonema ocellatum* SAG48.90**	Spheroidal vesicles arranged into filament. Branching filament surrounded by a sheath. T-type branching.	*Cells* 8.66 – 19.36 µm; *Trichome width* 15.54 – 19.36 µm; *Sheath width* 22.61 – 29.28 µm	/	Composed of polysaccharides mainly composing the sheath around filament. Detection of amide groups (nucleic acid and proteins).
***Bangiopsis franklynottii* CCMP3416**	Discoidal cells individually surrounded by a sheath and grouped together into a filament by common mucilage. T-type branching.	*Cells* 4.68 x 6.16 – 12.08 x 13.98 µm; *Trichome width* 9.5 – 35.46 µm ; *Mucilage width* 10 – 44.69 µm	Trilayered mucilage with the outer and inner electron-dense layers and a middle electron-tenuous layer. Thick laminated cell wall embedded in mucilage.	Detection of polysaccharides composing the mucilage surrounding the cells. Detection of C-O-C vibrations of the 3,6anhydrobridge (galactose) found in carrageenan (sulfated polysaccharide).

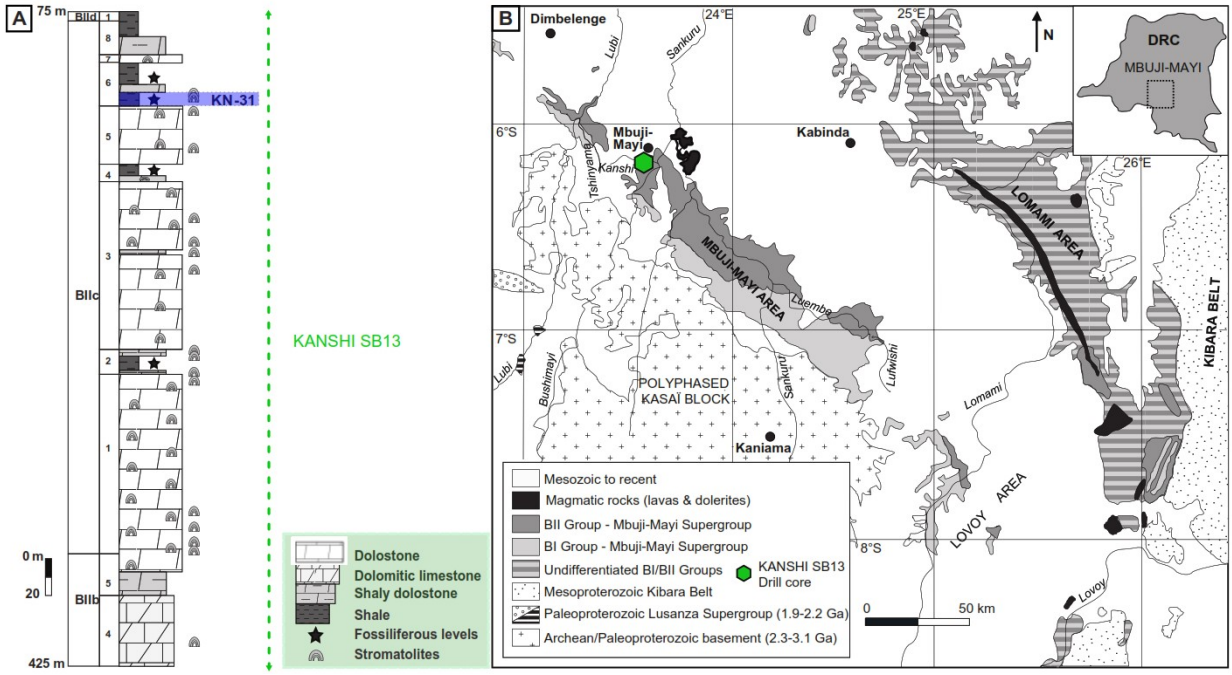

Figure S18. Geological context of studied samples, related to the STAR methods. (A) Stratigraphy of the drill core KanshiSB13 and the location (KN-31) of the samples of *P. filiformis*. **(B)** Geological maps of the Sankuru-Mbuji-Mayi-Lomami-Lovoy basin and the location of the Kanshi SB13 drill core. Modified from Sforna et al. (2022) [8].

Supplementary references

1. Petrov, P. Y., Sharma, M., Vorob'eva, N. G., and Sergeev, V. N. (2019). Facies-stratigraphic distribution of organic-walled and silicified microfossils in the early Billiyakh Basin (Lower Riphean, Anabar Uplift, Siberia). Paleontol. J., *53*(8), 867-872.
2. Vorob'eva, N. G., Sergeev, V. N., and Petrov, P. Y. (2015). Kotuikan Formation assemblage: a diverse organic-walled microbiota in the Mesoproterozoic Anabar succession, northern Siberia. Precambrian Res., *256*, 201-222.
3. François, C., Baludikay, B. K., Debaille, V., Birck, J. L., Limmois, D., Jourdan, F., Baudet, D., Paquette, J. L., Delvaux, D., and Javaux, E. J. (2023). Multi-method dating constrains the diversification of early eukaryotes in the Proterozoic Mbuji-Mayi Supergroup of the DR Congo and the geological evolution of the Congo Basin. Journal of African Earth Sciences, *198*, 104785.
4. Timofeev, B. V., Hermann, T. N., and Michailova, N. S. (1976). Mikrofitofossiliidokembria, kembriaiordovika (Microphytofossils of the Precambrian, Cambrian and Ordovician). *Nauka, Leningrad*, Scientific Institute of Precambrian Geology and Geochronology, 106 p [in Russian].
5. Han, C. M., Chen, L., Li, G. J., Pang, K., Wang, W., Zhou, G. Z., Yang, L., Lyu, W. G., Wang,K., Zhong, Z. H., Wu, C. X., and Yang, F. J. (2021). First record of organic-walled microfossils from the Tonian Shiwangzhuang Formation of the Tumen Group in western Shandong, North China. Palaeoworld, *30*(2), 208-219.
6. Vorob'eva, N. G., Sergeev, V. N., and Knoll, A. H. (2009). Neoproterozoic microfossils from the northeastern margin of the East European Platform. J. Paleontol., *83*(2), 161-196.
7. Baludikay, B. K., François, C., Sforna, M. C., Beghin, J., Cornet, Y., Storme, J. Y., Fagel, N., Fontaine, F., Littke, R., Baudet, D., Delvaux, D., and Javaux, E. J. (2018). Raman microspectroscopy, bitumen reflectance and illite crystallinity scale: comparison of different geothermometry methods on fossiliferous Proterozoic sedimentary basins (DR Congo, Mauritania and Australia). Int. J. Coal Geol., *191*, 80-94.
8. Sforna, M. C., Loron, C. C., Demoulin, C. F., François, C., Cornet, Y., Lara, Y. J., Grolimund, D., Sanchez, D. F., Medjoubi, K., Somogyi, A., Addad, A., Fadel, A., Compère, P., Baudet, D., Brocks, J. J., and Javaux, E. J. (2022). Intracellular bound chlorophyll residues identify 1 Gyr-old fossils as eukaryotic algae. Nat. comm., *13*(1), 1-8.
9. Movasaghi, Z., Rehman, S., and urRehman, D. I. (2008).Fourier transform infrared (FTIR) spectroscopy of biological tissues. Appl. Spectrosc. Rev., *43*(2), 134-179.
10. Alstadt, K. N., Katti, D. R., and Katti, K. S. (2012). An *in situ* FTIR step-scan photoacoustic inverstigation of kerogen and minerals in oil shale. Spectrochim. Acta A Mol. Biomol. Spectrosc. *SPECTROCHIM ACTAA 89,* 105-113.
11. Marshall, C. P., Javaux, E. J., Knoll, A. H., and Walter, M. R. (2005). Combined micro-Fourier transform infrared (FTIR) spectroscopy and micro-Raman spectroscopy of Proterozoic acritarchs: a new approach to palaeobiology. Precambrian Res., *138*(3-4), 208-224.
12. Borjas Esqueda, A., Gardarin, C., and Laroche, C. (2002). Exploring the diversity of red microalgae for exopolysaccharide production. Marine drugs, *20*(4), 246.
13. Liang, C. Y., and Marchessault, R. H. (1959). Infrared spectra of crystalline polysaccharides. I. Hydrogen bonds in native celluloses. J. Polym. Sci., *37*(132), 385-395.
14. Kaplan Can, H., Gurbuz, F., and Odabaşı, M. (2019). Partial characterization of cyanobacterial extracellular polymeric substances for aquatic ecosystems. Aquat. Ecol., *53*(3), 431-440.
15. Kansiz, M., Heraud, P., Wood, B., Burden, F., Beardall, J., and McNaughton, D. (1999). Fourier transform infrared microspectroscopy and chemometrics as a tool for the discrimination of cyanobacterial strains. Phytochemistry, *52*(3), 407-417.

16. Wang, Q., Ye, J. B., Yang, H. Y., and Liu, Q. (2016). Chemical composition and structural characteristics of oil shales and their kerogens using Fourier Transform Infrared (FTIR) spectroscopy and solid-state 13C Nuclear Magnetic Resonance (NMR). Energy & Fuels, *30*(8), 6271-6280.
17. Gómez-Ordóñez, E., and Rupérez, P. (2011). FTIR-ATR spectroscopy as a tool for polysaccharide identification in edible brown and red seaweeds. Food hydrocoll., *25*(6), 1514-1520.
18. Murdock, J. N., and Wetzel, D. L. (2009). FT-IR microspectroscopy enhances biological and ecological analysis of algae. Applied Spectroscopy Reviews, *44*(4), 335-361.
19. Sekkal, M., Huvenne, J. P., Legrand, P., Sombret, B., Mollet, J. C., Mouradi-Givernaud, A., andVerdus, M. C. (1993). Direct structural identification of polysaccharides from red algae by FTIR microspectroscopy I: Localization of agar in *Gracilaria verrucosa,* sections. Mikrochim. Acta*, 112,* 1-10.
20. Lin, R., and Ritz, G. P. (1993). Studying individual macerals using IR. microspectroscopy, and implications on oil versus gas/condensate proneness and “low-rank” generation. Org. Geochem., *20(6),* 695-706.
21. Coates, J. (2000). “Interpretation of infrared spectra, a practical approach” in Encyclopedia of analytical chemistry, John Wiley & Sons Ltd, 2000, R. A., Meyers, Ed. pp. 10815-10837.
22. Varnali, T., Edwards, H. G. M., and Hargreaves, M. D. (2009). Scytonemin: molecular structural studies of a key extremophilic biomarker for astrobiology. Int. J. Astrobiol., *8(2),* 133-140.
23. Larkin, P. (2011). Infrared and Raman spectroscopy principles and spectral interpretation. Elsevierpp. 230.
24. Grant, C. S., and Louda, J. W. (2013). Scytonemin-imine, a mahogany-colored UV/Vis sunscreen of cyanobacteria exposed to intense solar radiation. Organic geochem., *65*, 29-36.
25. Benning, L. G., Phoenix, V. R., Yee, N., and Tobin, M. J. (2004). Molecular characterization of cyanobacterial silicification using synchrotron infrared micro-spectroscopy. Geochim. Cosmochim. Acta, *68*(4), 729-741.
26. Ahmad, S., Kothari, R., Pathak, V. V., and Pandey, M. K. (2019). Fuel quality index: a novel experimental evaluation tool for biodiesel prepared from waste cooking oil. Waste and Biomass Valorization, *10*(8), 2237-2247.